Capillarity

Vol. 12, No. 3, p. 57-71, 2024

Original article

# MicroGraphNets: Automated characterization of the micro-scale wettability of porous media using graph neural networks

Mohammed K. Alzahrani, Artur Shapoval, Zhixi Chen, Sheikh S. Rahman*

*School of Mineral and Energy Resources Engineering, University of New South Wales, Kensington NSW 2033, Australia*

**Keywords:**
Porous media
wettability characterization
interfacial properties
artificial intelligence
deep learning
graph neural networks

**Cited as:**
Alzahrani, M. K., Shapoval, A., Chen, Z., Rahman, S. S. MicroGraphNets: Automated characterization of the micro-scale wettability of porous media using graph neural networks. Capillarity, 2024, 12(3): 57-71.
https://doi.org/10.46690/capi.2024.09.01

**Abstract:**
This study introduces MicroGraphNets, a deep learning framework for automating the microscopic characterization of wettability in porous media using graph neural networks. The framework predicts rock surface roughness, fluid/fluid interfacial curvatures, and contact angles at 3-phase contact lines from segmented multiphase micro-computed tomography images. This is achieved by converting these images into sets of surface and interfacial points, with their intersection defining the 3-phase contact line points. Specialized geometrical training graphs are constructed from these points to predict each property, leveraging surface and interfacial normal vectors as input features for constructing surface and interfacial graphs. To address the unique challenge that arises from the coexistence of all phases around 3-phase contact lines, distinct node types assigned to each phase were embedded as node features for constructing contact angle graphs. To predict the properties, the framework employs a message-passing graph neural network with three modules: an encoder for initial feature embeddings, a processor for aggregating neighboring embeddings and propagating messages, and a decoder for final property prediction. This approach effectively captures node and edge relationships, facilitating accurate regression of surface and interfacial properties. Validation includes testing on unseen samples and a synthetic droplet test against analytical solutions. Time-resolved analysis was performed to demonstrate the scalability and efficiency of the framework on large datasets. MicroGraphNets demonstrates superior accuracy and efficiency compared to traditional deep learning methods, showcasing its potential for predicting microscopic surface and interfacial properties of porous media.

## 1. Introduction

Wettability, which is the relative affinity of a surface for multiple coexisting fluids, underpins numerous multiphase processes related to water resource management and designing various engineering solutions for contaminant remediation in groundwater aquifers (Haines, 1930; Lourenço et al., 2018), geological carbon storage and sequestration in subsurface reservoirs (Iglauer et al., 2015), and hydrocarbon recovery by implementing innovative chemical Enhanced Oil Recovery techniques (Ding et al., 2019; Boampong et al., 2023; Shapoval et al., 2023). Additionally, understanding wettability is essential for unraveling the complex interactions between fluids and the internal surfaces of porous media (Shapoval et al., 2022).

Examination of the wettability of porous surfaces can be performed across many scales, including nano, molecular, micro (pore), macro (core), and field (reservoir) scales (Armstrong et al., 2021), providing insights into the complex nature of wettability and its diverse implications. Comprehensive characterization of wettability requires computations of various multiphase estimates that indicate the state of wettability of porous media, such as in-situ fluid/fluid interfacial

Yandy Scientific Press

*Corresponding author.
*E-mail address*: mohammed_khaled_a.alzahrani@unsw.edu.au (M. K. Alzahrani); a.shapoval@unsw.edu.au (A. Shapoval); zhixic@unsw.edu.au (Z. Chen); sheik.rahman@unsw.edu.au (S. S. Rahman).

Received March 19, 2024; revised April 25, 2024; accepted May 13, 2024; available online May 22, 2024.

curvatures and contact angles formed by the interface of fluids on the studied surface. The relationship between the interfacial curvature and the phase capillary pressure is described by the following Young-Laplace equation:

$$P_c = P_{nw} - P_w = \gamma\left(\frac{1}{R_1} + \frac{1}{R_2}\right) \quad (1)$$

where $P_c$, $P_{nw}$ and $P_w$ are the capillary, non-wetting phase, and wetting phase pressures, respectively, $\gamma$ is the interfacial tension between fluid phases, and $R_1$ and $R_2$ are the principal radii of the fluid/fluid interfacial curvature. Moreover, the following Laplace equation governs the balance between the surface and interfacial tensions at the contact points, and its relationship with the formed contact angles:

$$\gamma_{s/nw} - \gamma_{s/w} = \gamma_{w/nw}\cos\theta \quad (2)$$

where $\gamma_{s.nw}$, $\gamma_{s/w}$ and $\gamma_{w/nw}$ refer to the tensions between the solid surface and non-wetting phase, solid surface and wetting phase, and wetting phase and non-wetting phase, respectively, and $\theta$ is the contact angle between the fluid phases measured typically in the denser phase. Furthermore, the impact of surface roughness on wettability has been acknowledged in numerous studies because it can introduce contact angle hysteresis and non-wetting phase trapping (AlRatrout et al., 2018; Zulfiqar et al., 2020; Geistlinger et al., 2024).

At the microscopic scale, also known as the pore scale, which forms the focus of this study, micro-computed tomography (micro-CT) imaging technology has emerged as a transformative tool for visualizing immiscible fluid configurations within porous media (Zou and Sun, 2020). This technology has revolutionized the imaging of in-situ multiphase interactions, enabling the precise quantification of essential multiphase properties from reconstructed 3-dimensional (3D) images. The emergence of micro-CT has paved the way for researchers to develop state-of-the-art techniques for computing the multiphase properties with the highest possible accuracy. Early computation methods relied on random manual sampling and the computation of in-situ contact angles from images around the 3-phase contact lines (CL). However, this method is time-consuming, prone to user and selection biases, and results in a limited number of computations that may not be representative of the overall wettability. Later, an automated method for measuring contact angles was developed by directly using segmented images to obtain vectors normal to the fluid/fluid interface and rock surface at voxels belonging to the CLs and using their dot product to compute the contact angles (Klise et al., 2016). To date, the most robust numerical computation method published by AlRatrout et al. (2017) can be used to compute the surface roughness, fluid/fluid interfacial curvatures, and in-situ contact angles. This approach provides additional accuracy because it uses smoothed meshes representing all interfaces to compute the interfacial properties, thereby reducing the effect of voxelization on computed normals.

Deep Learning (DL) models, a subset of Artificial Intelligence, characterized by their ability to automatically learn patterns from complex data, have gained prominence as effective tools in multiple applications such as facial recognition (Balaban, 2015; Singh et al., 2019) and natural language processing (Deng and Liu, 2018; Wang and Gang, 2018) tasks. The majority of DL applications in microscopic porous media use Convolutional Neural Networks (CNNs), which have been employed to automate the processing of raw micro-CT images (Ar Rushood et al., 2020; Cao et al., 2020; Wang et al., 2021; Alqahtani et al., 2022), reconstruction of porous media (Wang et al., 2018), and characterization of subsurface rock properties (Alqahtani et al., 2020, 2021; Rabbani et al., 2020; Santos et al., 2020). The application of such approaches in wettability characterization can be exemplified by the work of Yun et al. (2020), which utilized CNNs to classify wettability from 2-dimensional (2D) images of micromodels. Regardless of the high accuracy achieved by this implementation, the developed model does not allow comparative analysis because it produces binary outputs, where 0 = water-wet and 1 = oil-wet. In addition, they cannot characterize mixed-wet (intermediate-wet) conditions, which have been shown to affect spontaneous imbibition in heterogeneous porous media (Diao et al., 2021). More recently, Rabbani et al. (2023) proposed DeepAngle, an Artificial Neural Network (ANN)-based model for estimating in-situ contact angles. In this approach, the sparsity of the contact angle measurements within the 3D images is handled by sampling spheres of varying sizes from different locations on the 3-phase CL. The sampled spheres were then flattened and fed into a feedforward ANN to predict contact angles through regression. These approaches, which are powerful for learning local features within predefined receptive fields from structured datasets, possess inherent limitations, such as their ability to operate exclusively on uniform (structured) grids, fixed input size, and the demand for substantial memory and computational resources.

In contrast to the aforementioned techniques, some DL models can learn from unstructured data such as point clouds, meshes, and graphs, and have emerged as promising alternatives for pore-scale modelling. Examples of these methods include PointNet (Charles et al., 2017) and Graph Neural Networks (GNNs). Such methods have the potential to overcome the constraints of structured approaches and offer versatility in handling complex porous media modelling tasks. Most published works related to the application of these methods aim to develop and train models to predict pore-scale flow properties such as permeability. For instance, point clouds have been used to model rock surfaces and train PointNet architectures to predict the absolute permeability of porous media (Kashefi and Mukerji, 2021). On the other hand, Cai et al. (2023) extracted Morse graph representations of porous media and trained equivariant GNNs, while Alzahrani et al. (2023) utilized pre-trained CNN-based features to construct graphs for training GNNs to predict the permeability. Moreover, GNNs have recently been employed to predict elastic moduli from digital rock images (Chung et al., 2024). To the best of our knowledge, there are no published methods that use unstructured data as inputs for training DL models to characterize the pore-scale wettability of porous media.

In this paper, we present MicroGraphNets, a DL framework that automates microscopic characterization of porous media using GNNs. This study contributes to the expanding number of techniques available for analyzing the in-situ wettability

**Table 1**. Summary of porous media properties used for training and testing.

| Rock name | Type | Wetting state | $\varphi$ (%) | $S_w$ (%) | $\theta_{mean}$ (Degrees) | $k_{mean}$ (1/μm) | $R_{mean}$ (μm) | Dataset |
|---|---|---|---|---|---|---|---|---|
| Bentheimer (BH) | Sandstone | Water-wet | 22.8 | 92.9 | 58.1 | 0.0333 | 1.152 | Training |
| Indiana limestone (IL) | Carbonate | Oil-wet | 13.4 | 69.1 | 124.9 | -0.0117 | 1.007 | Training |
| Luxembourg (LUX) | Sandstone | Water-wet | 7.9 | 81.2 | 66.8 | -0.0088 | 0.963 | Testing |
| | | Mixed-wet | 8.7 | 35.2 | 96.8 | 0.0131 | 0.379 | Testing |
| Ketton limestone (KL) | Carbonate | Water-wet | 11.0 | 59.7 | 61.6 | 0.0035 | 1.340 | Testing |

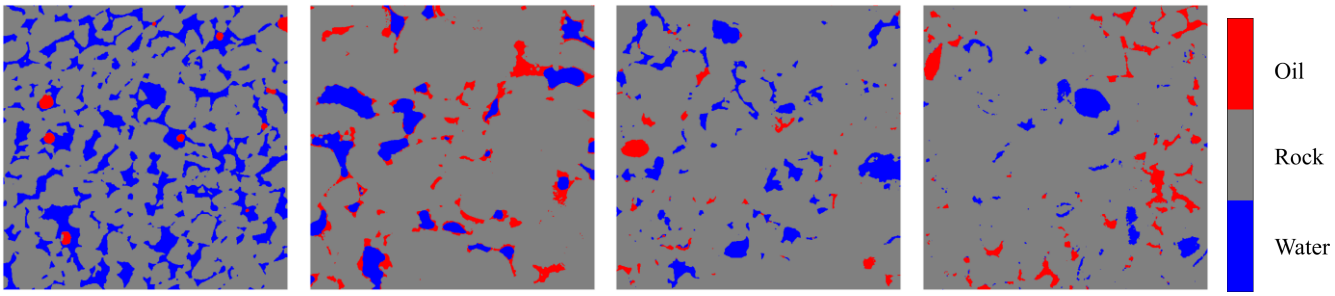


**Fig. 1**. Visualizations of 2D slices of porous media. (a) BH, (b) IL, (c) LUX-WW and (d) LUX-MW.

of porous media and its related properties. The remainder of this paper is organized as follows: In the Methods section, we describe the datasets used for training, validation, and testing; numerical methods used for computing the actual, also referred to as ground truth (GT); surface and interfacial properties; graph construction approaches; MicroGraphNets architecture; and training and testing procedures. The results are then discussed, including the training, validation, and testing performance; comparison with analytical synthetic droplet test solutions; and testing on unseen samples. Moreover, a time-resolved analysis of the dynamic contact angles throughout the waterflooding experiment is included, along with a discussion of the memory and computational requirements. Finally, we conclude and recommend directions for future research.

## 2. Methods

### 2.1 Training and testing datasets

The training dataset used in this study comprised two micro-CT images of rock samples with varying structures and wetting characteristics: Water-wet Bentheimer (BH) sandstone (Sun et al., 2020) and oil-wet Indiana limestone (IL) (Shapoval et al., 2022; Alzahrani et al., 2023). Micro-CT images were acquired for both samples at residual oil saturations of 94% and 87% for the BH and IL, respectively. These samples satisfied the main requirement for building the dataset, which was to build a dataset that included all possible values within the ranges of estimates of the surface and interfacial properties. The grayscale (raw) micro-CT images were segmented using the watershed algorithm (Meyer and Beucher, 1990) into 0 = water (dense phase), 1 = matrix (solid phase), and 2 = oil (light phase). Visualizations of 2D slices of porous media is shown in Fig. 1 Accurate image processing and phase segmentation are vital for the accuracy of the numerical computation of multiphase properties (Garfi et al., 2020).

In addition, to assess the robustness of the developed models when encountering samples that were not included during training, that is, unseen samples, two additional samples, namely Luxembourg (LUX) sandstone samples, were used to test the trained models. These sandstone samples represent distinct wetting conditions, one being water-wet (LUX-WW) and the other exhibiting mixed wetting characteristics (LUX-MW), to align with the diversity in wetting characteristics covered by the training dataset. Finally, published images of time-resolved flooding experiments performed on a Ketton limestone (KL) sample were used to test the performance of the trained model on large volumes of data (Rücker et al., 2019). The relevant rock and interfacial properties of the samples used in this study are summarized in Table 1.

### 2.2 Numerical pore-scale wettability characterization methods

In this study, we used the automatic mesh-based method proposed by AlRatrout et al. (2017) to compute the GT values of the surface and interfacial properties. In this approach, a multi-zonal mesh is extracted from the segmented multiphase images, where the first zone ($z_1$) represents the interface between the lighter phase and the solid surface (oil/rock), the second zone ($z_2$) represents the fluid/fluid (oil/water) interface, and the third zone ($z_3$) represents the interface between the denser phase and the solid surface (water/rock). These meshes were smoothed using volume- and curvature-preserving Gaussian smoothing to minimize the effect of voxelization on the

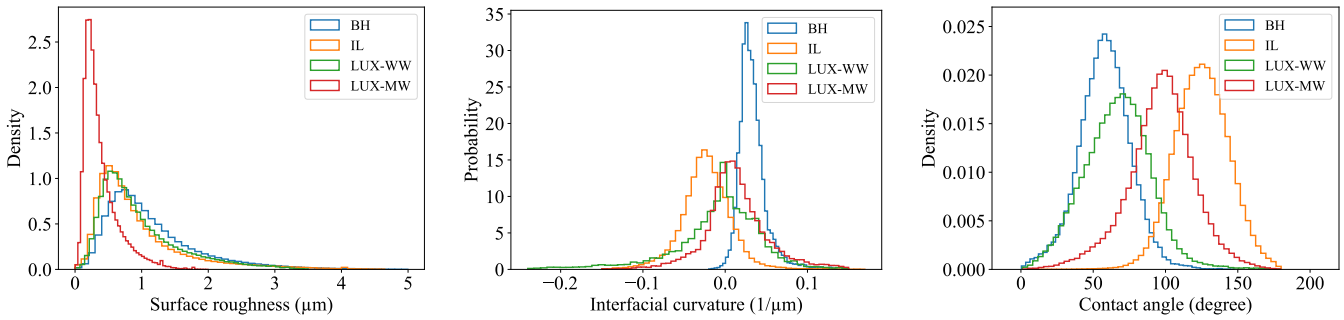


(a) (b) (c)

**Fig. 2**. Probability distributions of the GT (a) surface roughness, (b) interfacial curvatures and (c) contact angles of different rocks computed using the automated method proposed by AlRatrout et al. (2017).

measurements. Subsequently, normal vectors were computed at every location on the meshes. The curvature at every vertex on the extracted mesh can be computed as the sum of the dot product of the vertex normal and a vector normal to the contact line and tangent to the fluid/fluid interface, measured in 1/μm. The computed curvatures of the rock surface can be used to compute the surface roughness at each vertex using the following relationship proposed by (AlRatrout et al., 2018):

$$R_{a_i} = \frac{1}{N_{adj}} \sum_{j \in adj(i)}^{N_{adj}} \left| k_j a_j \right| \tag{3}$$

where $R_{a_i}$ is the surface roughness at vertex $i$, measured in μm, $k_j$ and $a_j$ are the computed surface curvatures and areas, respectively, of vertices $j$ which are adjacent to node $i$, denoted $j \in adj(i)$, and $N_{adj}$ is the number of adjacent vertices. In this method, the modulus of curvature is used; hence, the $R_{a_i}$ values are always positive, and indicate how rough the rock surface is at vertex $i$.

Finally, the contact angles were computed at every vertex belonging to the 3-phase CL. This was accomplished by calculating the dot product of the vectors normal to the oil/water and water/rock interfaces, enabling the measurement of the contact angles that enclose the denser phase (water). The following equation was used to compute the contact angle for each vertex belonging to the 3-phase CL:

$$\theta_i = \pi - \cos^{-1}\left( \mathbf{n}_i|_{z_2} \cdot \mathbf{n}_i|_{z_3} \right) \tag{4}$$

where $\theta_i$ is the contact angle calculated at every vertex $i$ on the 3-phase CL and $\mathbf{n}_i|_{z_2}$ and $\mathbf{n}_i|_{z_3}$ are the normals at $i$ belonging to $z_2$ and $z_3$, respectively. This approach resulted in three sets of data, each including 3D spatial coordinates, along with the corresponding surface roughness, interfacial curvatures, and in-situ contact angles. The probability distributions of the surface and interfacial properties computed using this method are shown in Fig. 2. Visualizations of the spatial distributions of these properties throughout the samples are shown in Fig. 3.

After performing the numerical computations of the multi-phase estimates, three sets of points were obtained: (1) Surface points, (2) interfacial points and (3) 3-phase contact line points, which contain the spatial coordinates in 3D space along with the computed surface roughness at set (1), interfacial curvatures at set (2), and contact angles at set (3). These sets of points are ready for use as inputs for the graph construction module, as explained in the next section.

## 2.3 Graph construction module

Generally, a graph is represented by $G = \{V, E\}$ where $G$ is the graph, $V$ is the set of nodes, and $E$ is the set of edges connecting the nodes. Computationally, graphs are represented by a set of matrices, defined by $G = \{\boldsymbol{A}, \boldsymbol{X}, \boldsymbol{E}\}$ where $\boldsymbol{A}$ is the adjacency matrix, which is a binary matrix of shape $[n \times n]$, where $n$ is number of nodes, that captures the connectivity between nodes, while $\boldsymbol{X}$ is node features matrix, of shape $[n \times n_f]$, where $n_f$ is the number of node features, and $\boldsymbol{E}$ is the edge attributes (features) matrix, of shape $[n_E \times n_{attr}]$ where $n_E$ and $n_{attr}$ represent the number of edges and edge attributes, respectively. To refer to a single feature vector of node $i$ and an edge feature vector between nodes $i$ and $j$, $x_i$ and $e_{ij}$ notations are used, respectively. Graph edges can be directed or undirected, however, in this study, all graphs were constructed with undirected edges, which means that if $e_{ij}$ exists, $e_{ji}$ must exist as well. The label matrix used for training the GNNs is represented by $Y$. The shape of $Y$ depends on the level at which the training task is performed, such as the node, edge, or graph level. All graphs in the present study are used for node-level prediction tasks, meaning that, given the node and edge input features, the models are trained to predict the final node embeddings that represent the desired output property. Specifically, a single output value (roughness, curvature, or contact angle) for each node is predicted, i.e., $Y$ is a vector of size $[n \times n_y]$, where $n_y$ is the size of a single prediction vector, which is set to 1 throughout this study, and each label for node $i$ is indicated by $\widehat{y}_i$. In the following sections, we describe the details of converting sets of surface points, interfacial points, and 3-phase CL neighborhood extracted from segmented multiphase images into graph representations based on the aforementioned graph definition.

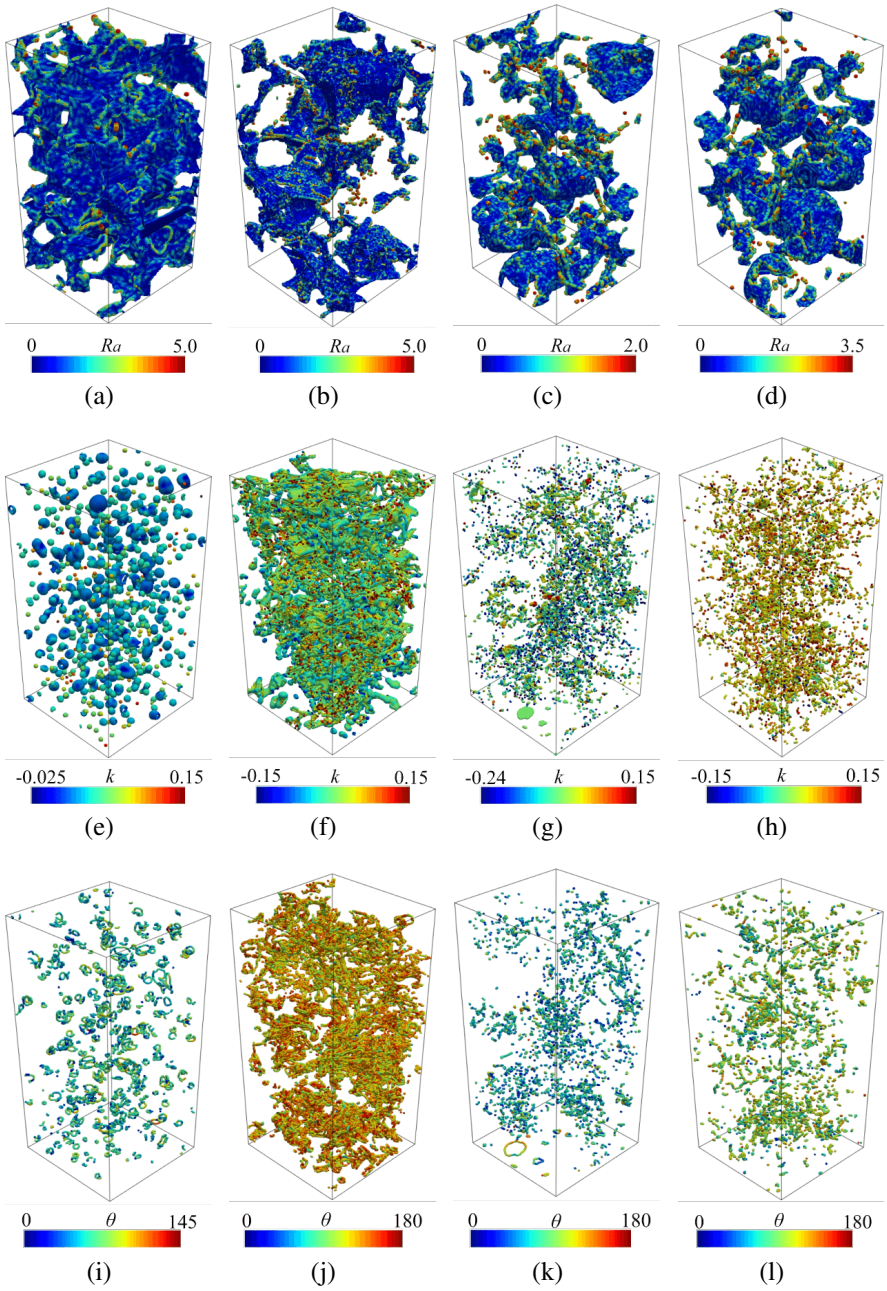


**Fig. 3**. 3D visualizations of the spatial distributions of (a)-(d) surface roughness, (e)-(h) interfacial curvatures and (i)-(l) contact angles. From left to right: BH, IL, LUX-WW, and LUX-MW.

### *2.3.1 Surface roughness and interfacial curvature graphs*

To construct graphs for training MicroGraphNets to predict the surface roughness and interfacial curvatures, we started by using the sets (1) for surface points and (2) for interfacial points resulting from the selected numerical method, along with the computed GT values of the roughness and interfacial curvature, respectively, as the graph nodes. These sets are visualized in the top and middle rows Fig. 3, respectively. Then, for every node $k$, the number of neighbors is searched and edges are constructed using the K-Nearest Neighbor (KNN) algorithm (Goldberger et al., 2004). For these graphs, k was selected as 10 through trial and error to achieve the best possible balance between the accuracy and efficiency. Moreover, because the aim was to build geometrical graphs that represent surfaces and interfaces in a geometric space, the geometrical information was embedded as edge attributes instead of node features, computed from the relative displacement vectors between all pairs of connected nodes concatenated with their norms, yielding $n_{attr} = 4$. Normals computed from KNN nodes using efficient techniques to construct local surfaces and compute the surface normal (Yu et al., 2019) were used as node input features, resulting in $\boldsymbol{X}$ of shape $[n \times 3]$.

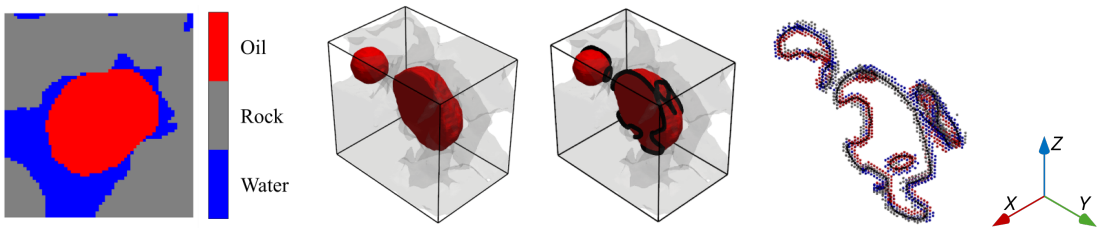


**Fig. 4**. Illustration of (a) 2D slice of a trapped oil blob, (b) 3D volume showing the blob where red is oil, gray is rock, and water is transparent, (c) identified 3-phase contact line neighborhood drawn in black and (d) identified sets of points in the neighborhood of 3-phase CL, where red represents oil points, gray represents rock points, blue represents water points, and black represents the identified 3-phase CL points.

**Table 2**. The network and training hyper-parameters.

| Type | Parameter | Value |
|---|---|---|
| Network hyper-parameters | Hidden layer size | 16 |
| | $L$ | 10 |
| | Aggregation function | Sum |
| Training hyper-parameters | Learning rate | 0.001 |
| | Batch size | 32 |
| | Optimizer | Adam |

### 2.3.2 Contact angle graphs

In this scenario, graph construction is not as straightforward for the following reasons:

1) Contact angle computation requires spatial information (coordinates and normals) from both interfaces, namely, the rock surface and fluid/fluid interfacial nodes around the 3-phase CLs,
2) the measurements are not performed at every node; instead, contact angles are measured only on the 3-phase CL,
3) normals cannot be computed on the 3-phase CLs, and hence, different node embedding strategies are needed.

To overcome these challenges, specialized graphs were built to represent the neighborhood points of the 3-phase CLs by performing numerous morphological dilations on the binary maps of the points of the 3-phase CLs. Node features were then set to represent different node types with values of 0, 1, 2, and 3, representing water, rock, oil, and 3-phase CL nodes, respectively. The identification of the 3-phase CLs as well as the points belonging to their neighborhood are illustrated in Fig. 4. To computationally represent the node types as inputs, one-hot encoded vectors of size four were used for each type, resulting in $n_f = 3$. Edges and edge attributes were constructed using the method described in the previous subsection. To overcome challenges (2) and (3), an arbitrary negative value, e.g., -999, was used as a label for neighboring nodes that do not belong to the 3-phase CL.

## 2.4 MicroGraphNets architecture

In this section, details of the MicroGraphNets architecture are explained. Our model comprises three main modules: (1) Encoder, (2) processor and (3) decoder modules. First, the encoder takes the initial node features and edge attributes, along with the edge index matrices, and generates node and edge embeddings, as described by the following equation:

$$\mathrm{ENC} = \mathrm{ReLU}\left[\mathrm{MLP}(\boldsymbol{A}, \boldsymbol{X}, \boldsymbol{E})\right] \tag{5}$$

where ENC is the output of the encoder (learned embeddings), MLP represents the multilayer perceptron, an ANN with multiple neurons in the hidden layers, and ReLU is Rectified Linear Unit used as the activation layer. For simplicity, the size of the hidden layers was chosen to be constant across all the tasks. An optional normalization layer can be applied to the final encoder output. Second, the processor module comprises $L$ duplicate message-passing layers, which are considered the fundamental operations for building GNNs. The size of the hidden layer and the number of processor layers are hyperparameters that influence the model performance and training efficiency. A summary of the selected network hyperparameters is presented in Table 2. These hyperparameters were selected after trial and error to achieve the best balance between accuracy and computational efficiency. The processor comprises three functions: (a) A message construction function that collects neighboring node embeddings and generates a message as follows:

$$m_{i\to j} = \mathrm{msg}\left(h_i, h_j, e_{ij}\right) \tag{6}$$

where $m_{i\to j}$ is the calculated message between nodes $i$ and $j$; using the general form "msg" function, and $h_i$ and $h_j$ are the features of the source and target nodes, respectively. Secondly, in the (b) aggregation function:

$$m_i = \sum_{j\in N(i)} m_{j\to i} \tag{7}$$

where $m_i$ is the aggregated message from neighbors $j$ of node $i$, where the neighbors are denoted $N(i)$, and $m_{j\to i}$ is the message from node $j$ relating to node $i$. After aggregating the messages of all nodes, the update function (c) is applied. In this function, the embeddings are updated using the following

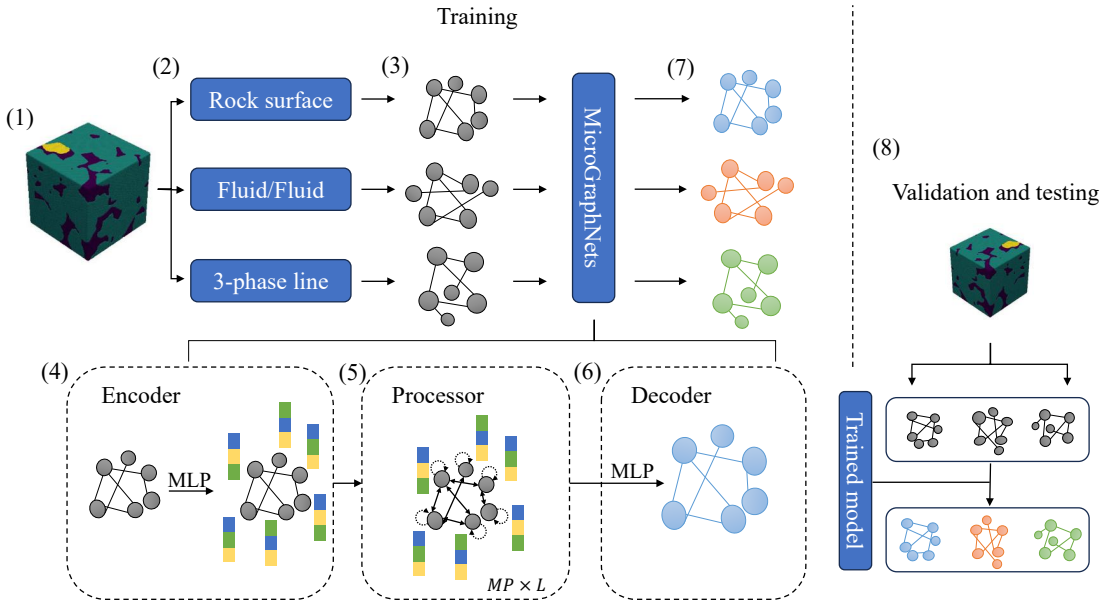


**Fig. 5**. Schematic diagram illustrating the architecture of the MicroGraphNets. The Figure shows (1) a segmented micro-CT subsample from which (2) the rock surface, fluid/fluid interface, and 3-phase CL points are extracted, and (3) the sets of points are converted into KNN graphs based on the methods explained in Section 3.3.3. Then, the graphs are used to train MicroGraphNets by passing them through (4) an encoder that uses MLPs to process the initial node and edge features to learn node embeddings, and (5) a set of $L$ processors that perform message passing, aggregation of messages, and updating the embeddings, and the final embedding is processed using the (6) processor's MLP into (7) the final output. Finally, (8) the trained models are validated and tested by constructing graphs for a test sample and passing them through the models.

equation:

$$h_i' = \text{update}\,(m_i, h_i) \tag{8}$$

where "update" is the general form function that takes in $m_i$ and $h_i$ and outputs $h_i'$, which is the updated embeddings of node $i$. In this implementation, the "msg" and "update" functions use ANN transformations, that is, MLPs.

Finally, the decoder decodes the final node embeddings by passing $h_i'$ through two MLPs separated by a ReLU. The shape of the output of the last layer in the decoder must be 1, such that every trained network accurately predicts a single value per node. A schematic of the overall architecture of the MicroGraphNets is shown in Fig. 5.

## 2.5 Training, validation and testing

To computationally perform GNN operations, both PyTorch (Paszke et al., 2019) and PyTorch Geometric (PyG) (Fey and Lenssen, 2019) open-source Python packages were utilized. These libraries provide functionalities for performing and optimizing resource-intensive DL operations. To facilitate training using PyTorch and PyG, edge information is saved in a COO matrix, called the edge index, of shape $[2 \times n_E]$, which is an efficient way to save edge information, namely, as source and target nodes. For surface roughness and interfacial curvatures, batch training was implemented by subsampling graphs from the roughness and interfacial curvature sets. This is optional for building graphs for contact angle prediction because measurements of angles are computed only at the 3-phase CL, making the graph sizes significantly smaller. However, for consistency, a constant subsample size of 100 cubic voxels was selected for all tasks. Selecting this size ensures that the graph construction time does not increase exponentially because of the significantly large graphs. The total number of training graphs resulting from the selection of this subsample size was 4,456. It is noteworthy that one of the advantages of GNNs is that they do not have to obey a fixed input size, such as CNNs, which makes them more versatile when testing on larger graphs while maintaining their generalizability.

In both cases, data were split into 70/20/10 for training, validation, and testing. The training set was used to train the model by running the MicroGraphNets model and then calculating the Mean Absolute Error (MAE) as the objective loss function, as shown by the following equation:

$$\text{MAE} = \frac{1}{N}\sum_{i=1}^{N} |y_i - \hat{y}_i| \tag{9}$$

where $N$ denotes the number of samples in the dataset, $y_i$ denotes the GT values, and $\hat{y}_i$ denotes model predictions. The MAE loss was minimized during backward propagation using the Gradient Descent approach (Amari, 1993) with the Adam optimizer (Kingma and Ba, 2017). A learning rate of 0.001 was used for all tasks, and the models were trained for 100 epochs for surface roughness and interfacial curvature predictions and 1,000 epochs for contact angle prediction. A summary of the training hyperparameters is provided in Table 2.

The model was validated during training by running the

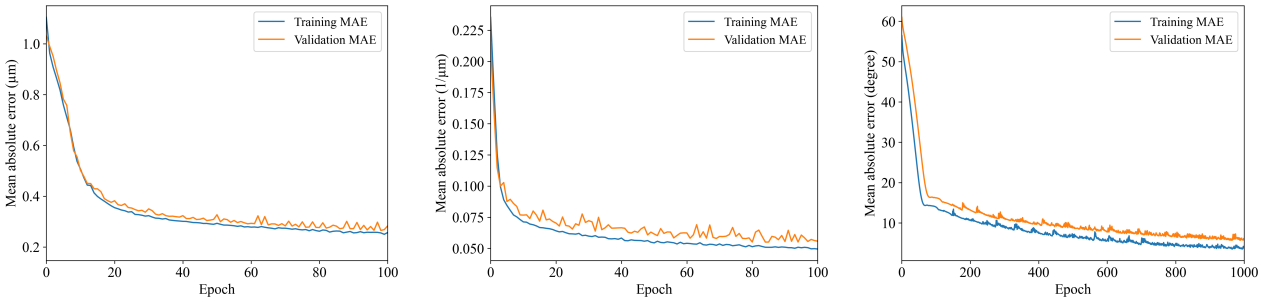


**Fig. 6**. Training and validation MAE losses of MicroGraphNets for predicting (a) surface roughness, (b) interfacial curvatures and (c) contact angles.

model on the validation dataset after each epoch and recording the validation loss. An early stopping strategy was implemented to avoid overfitting by terminating the training process if the validation loss failed to improve for the previous 10% of the total number of designated epochs and only the models that achieved the lowest validation loss were saved. In addition, after the training was completed, the performance of the trained models was tested on the test dataset, which comprised of samples that were not included in the training process. Moreover, the synthetic droplet test was utilized in the case of contact angles, which are commonly used to benchmark in-situ contact angle computation approaches. Finally, the efficiency of the model was tested by performing a time-resolved analysis of the contact angle on the KL sample obtained from a synchrotron micro-CT device (Rücker et al., 2019), which enabled the imaging of microscopic fluid flow at various time steps.

## 3. Results and discussion

In this section, the training, validation, and testing performance of the proposed architectures are presented. Subsequently, the synthetic droplet test results are discussed. Next, the results of testing the trained models on unseen samples, namely LUX-WW and LUX-MW sandstones, are discussed. Moreover, we show the interpretation of the time-resolved synchrotron images of the multiphase fluid flow experiments performed on the KL sample using MicroGraphNets. Finally, a discussion of the memory and computational requirements is provided.

### *3.1 Training, validation and testing performance*

The performances of the trained models were evaluated based on the MAE of predicting surface roughness, interfacial curvature, and contact angles separately after each training epoch. The MAE losses resulting from running the model on the training and validation datasets are recorded and illustrated in Fig. 6. These results indicate that the proposed architectures reduced the MAE losses to less than 0.21 μm, 0.057 1/μm, and 6° for the surface roughness, interfacial curvature, and contact angle predictions, respectively, for the validation samples. Visual comparisons between the ground truth and model predictions for the surface roughness and interfacial curvatures are shown in Fig. 7. The samples in this figure were obtained from the testing dataset, which was not encountered during training; however, they belong to the same rock types in the training dataset, namely BH and IL. In addition, the figure illustrates the absolute differences between the GT and predicted values, where lighter colors represent higher prediction errors. As shown in the figure, most of the high-error predictions are located near the edges of the selected samples, which is expected because these regions lose some neighbor information owing to random subsampling (cropping). In addition, the resulting probability distributions from the GT and predictions were compared, showing that a high match can be observed even on unseen samples. The most important values obtained from the probability distributions are the mean interfacial curvatures and surface roughness values, which also show a high match between the GT and predictions.

On the other hand, the performance of MicroGraphNets for predicting the in-situ contact angles of the testing samples is summarized in Figs. 8(a) and 8(b). These figures show the GT values of the contact angles plotted in a scatter plot against the predicted values. As illustrated in the figure, the model achieved coefficients of determination ($R^2$) of 0.968 and 0.923 for predicting the contact angles of the BH and IL testing samples, respectively. Similar to the prediction of the other properties, it can be observed that some model predictions were not accurate in both cases. Two reasons contributed to these inaccuracies: (1) Random cropping and (2) extremely low or high angles, because these measurements are less common in both datasets than moderate values, as shown in the GT probability distributions, Fig. 2.

### *3.2 Synthetic droplet test*

A common approach for evaluating contact angle measurement methods is the synthetic droplet test. This test was accomplished by generating a voxelized 3D image of a slanted surface and a spherical droplet placed on top of the surface to compare the contact angles from the proposed method with the analytical contact angles. Images with different angles were obtained by adjusting several parameters, such as droplet size,

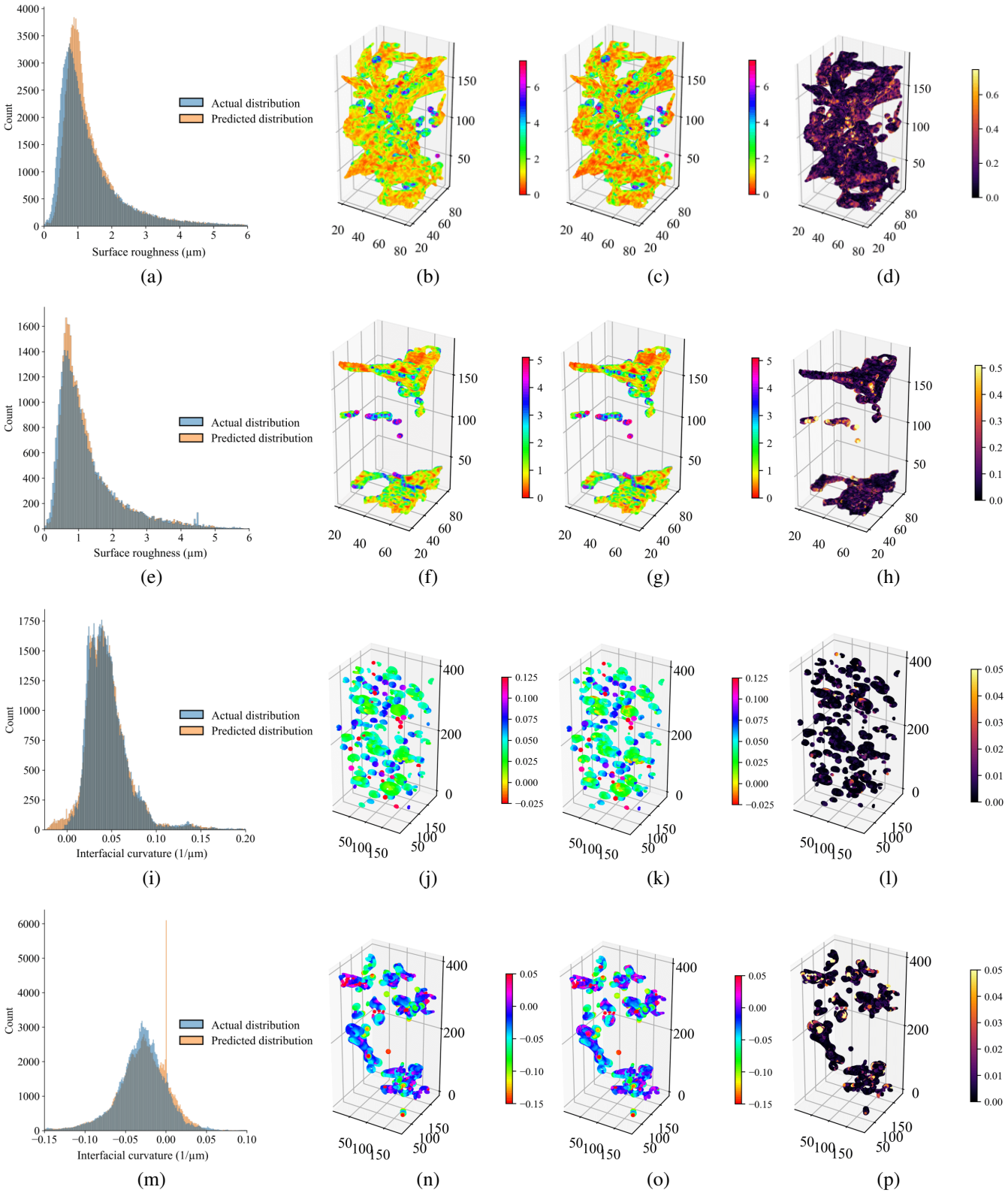


**Fig. 7**. Visualizations of the prediction results of the trained model on the testing samples showing (a)-(d) the surface roughness of the BH sample, (e)-(h) surface roughness of the IL sample, (i)-(l) interfacial curvature of the BH sample, and (m)-(p) interfacial curvature of the IL sample. From left to right, the figure shows the GT and predicted probability distributions, 3D spatial distributions of GT values, model predictions, and absolute differences.

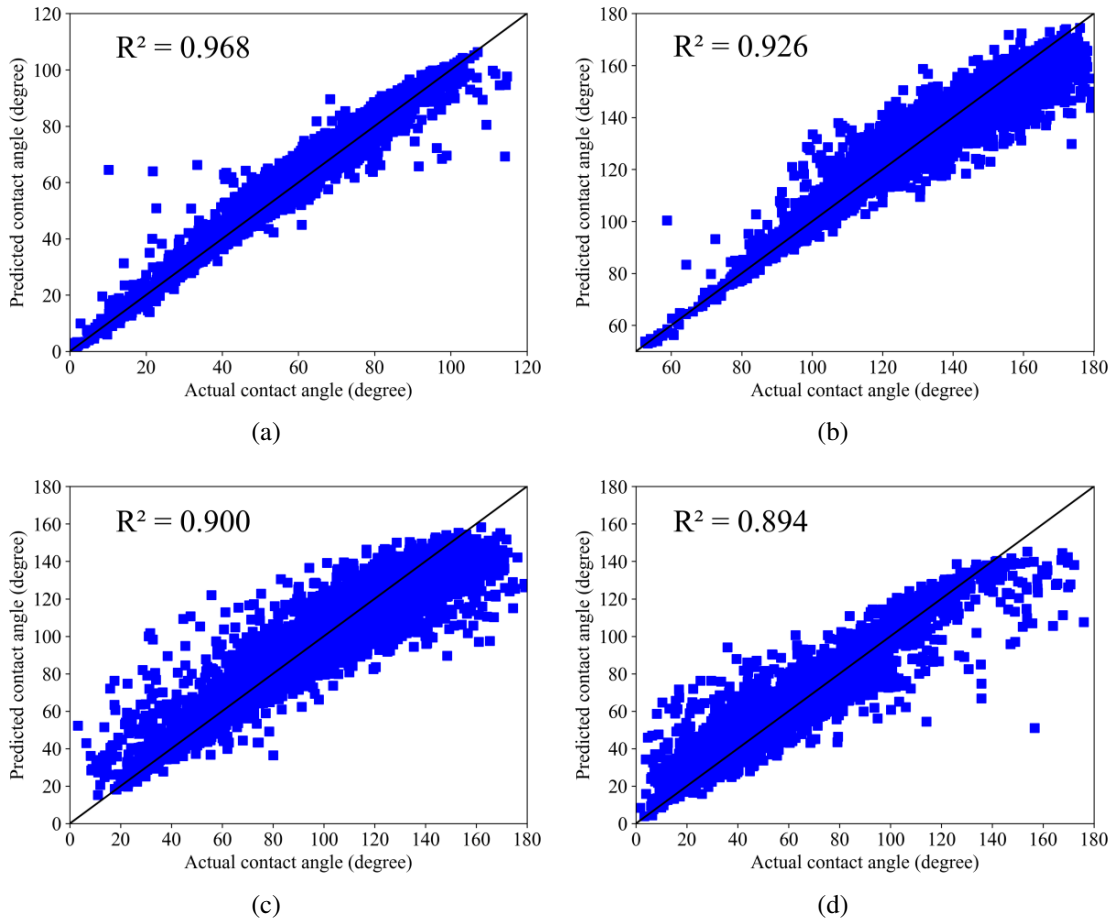


**Fig. 8**. Scatter plots illustrating GT vs predicted values of contact angles for testing samples, namely, (a) BH and (b) IL and samples of unseen rock types which are (c) LUX-WW and (d) LUX-MW.

center height, and resolution, as well as the tilt angle of the surface. The analytical contact angles were then calculated geometrically from these synthetic images. An example of the synthetic droplet test is shown in Fig. 9(a). In the present study, various combinations of the parameters, such that the entire range of contact angles was covered, from 0° to 180°. The results of this test are illustrated in Fig. 9(b) using the maximum, minimum, and mean of the predicted angles plotted against the analytical (actual) contact angles computed geometrically. As shown in the figure, the mean of the predicted contact angles closely matched the analytical solution represented by the dashed line.

### 3.3 Testing on unseen samples

In addition to the previous test, samples of unseen structures and interfacial properties were used to test the robustness of the proposed models, namely, LUX-WW and LUX-MW. With respect to the surface roughness and interfacial curvatures, Fig. 10 illustrates that the proposed model closely matches the GT values, even when tested on unseen samples. It is noteworthy that only one LUX sample, namely, the water-wet sample in this case, is illustrated for roughness prediction, as the surface roughness of the porous media will not be altered by changing the wetting characteristics. By contrast, in Figs. 8(c) and 8(d), the predicted contact angles are plotted against the GT angles for LUX-WW (left) and LUX-MW (right). As can be observed in the figure, the model achieved slightly lower accuracy than the samples of rock types that were included in the training process, that is, BH and IL. The resulting $R^2$ values were 0.900 and 0.894 for the water-wet and mixed-wet LUX samples, respectively. In addition, to inspect the effect of these inaccuracies on the overall characterization of the mean contact angles, the GT and predicted probability distributions of the contact angles of both LUX samples are illustrated in Fig. 11. The figures show that for these samples, the mean contact angles closely match regardless of the discrepancies caused by the extreme measurements.

### 3.4 Time-resolved analysis

In addition to the static contact angles captured at the end of the flooding experiments, the contact angle measurements can be performed dynamically using synchrotron micro-CT imaging, which allows the acquisition of tomographic data at different time steps during the experiment. To showcase one of the applications of the proposed model, we performed pre-

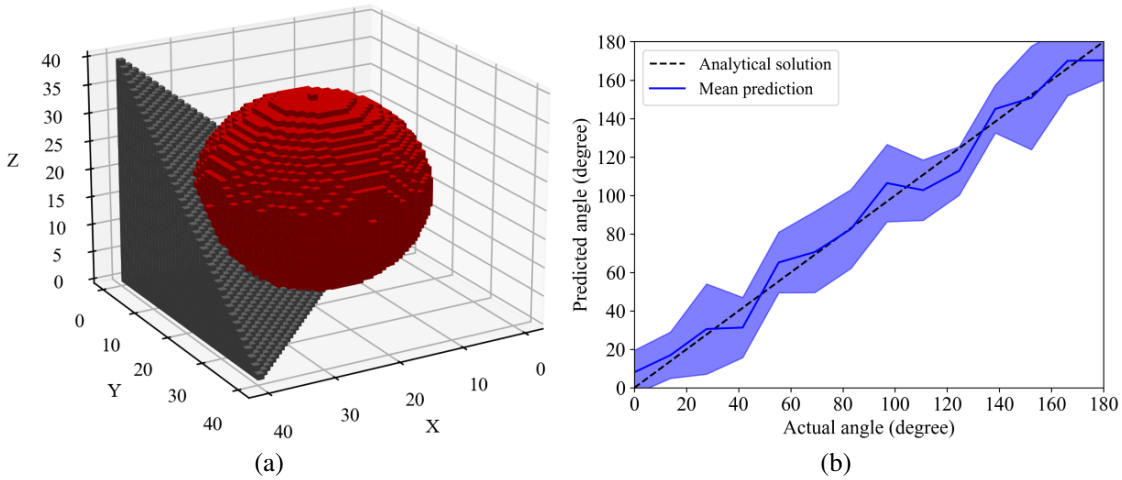


**Fig. 9**. Visualization of an example of (a) the synthetic droplet test with a surface slanted by 45° and (b) the results of predicting contact angles using MicroGraphNets plotted against the analytical solution of contact angles.

**Table 3**. Time and memory requirements of MicroGraphNets compared with numerical methods.

| Type | Inference time (s) | Memory (GB) |
|---|---|---|
| Numerical methods | 1,560 | 47 |
| MicroGraphNets | 967 | 28 |

dictions using synchrotron micro-CT images published by Rücker et al. (2019). In this specific case, a water-wet KL sample, initially at 26.6% water saturation, was flooded and images were obtained every 38 s until a water saturation of 59.7% was reached. The results of running the contact angle model on the images of the KL sample are summarized in Fig. 12. The figure shows (a) the resulting probability distributions of the contact angles at different time steps, distinguished by different colors. Moreover, (b) the mean contact angles predicted by the trained model were compared with the GT contact angles computed using the automated numerical computation method.

Two conclusions can be drawn from the results illustrated in Fig. 12. First, in a water-wet system, during the waterflooding experiment, the number of points of fluid/fluid contact at the rock surface was reduced with water injection time. This occurs because the injected water sweeps oil from large pores owing to the significantly larger number of water-filling events compared to oil-filling events, which occur in small pores where water is unable to overcome the entry pressure, enter the pore, and replace the oil. Second, this decrease in the number of points of contact, generally observed in large pores of water-wet systems where water-filling events dominate, causes the mean contact angle of the entire system to increase over time, as the oil ganglia present in small pores remain in contact with the pore surface.

## 3.5 Memory and computational requirements

One of the main challenges facing deep learning frameworks is the memory and computational resources required for training and inference. In the present study, even with the availability of these resources, some restrictions were encountered because large graphs are generally more memory-consuming than 3D structured grids (volumes). For instance, it was not possible to train the models on a single graph that includes all surface and interfacial points for training the model to predict surface roughness and interfacial curvatures, respectively, as such a graph cannot fit into the available 24 GB Graphical Processing Unit memory; therefore, a mini-batching technique was employed. Additionally, the number of nearest neighbors used to construct the graphs was carefully selected after trial and error to achieve the best possible balance between accuracy and reduction of required resources. Moreover, for graphs representing regions around the 3-phase contact line, the number of morphological dilations performed to capture the neighborhood is a hyperparameter that can influence the accuracy of the models. Selecting a small number of dilations, specifically less than four, causes the model to fail to generalize. However, selecting a high number of dilations, typically above eight, causes the graphs to be unnecessarily large and includes some regions that are not essential for predicting the contact angles.

With the selected hyperparameters discussed in the Methods section, and by applying the mini-batching technique, the models can be trained relatively efficiently for all tasks. Specifically, MicroGraphNets takes 2.3 and 1.7 minutes/epoch to be trained on predicting surface roughness and interfacial curvatures, respectively. However, because the number of dilated points surrounding the 3-phase CL is significantly smaller than the surface and interfacial points, training the model to predict the contact angles is much faster, requiring an average of 14 s/epochs and enabling longer training than other properties. After the training is completed, the inference of the contact angles on the testing samples by the trained models can be achieved efficiently using a single Graphical Processing Unit. Table 3 summarizes the time and memory required to obtain a full characterization of the surface roughness, interfacial curvatures, and contact angle measurements of the

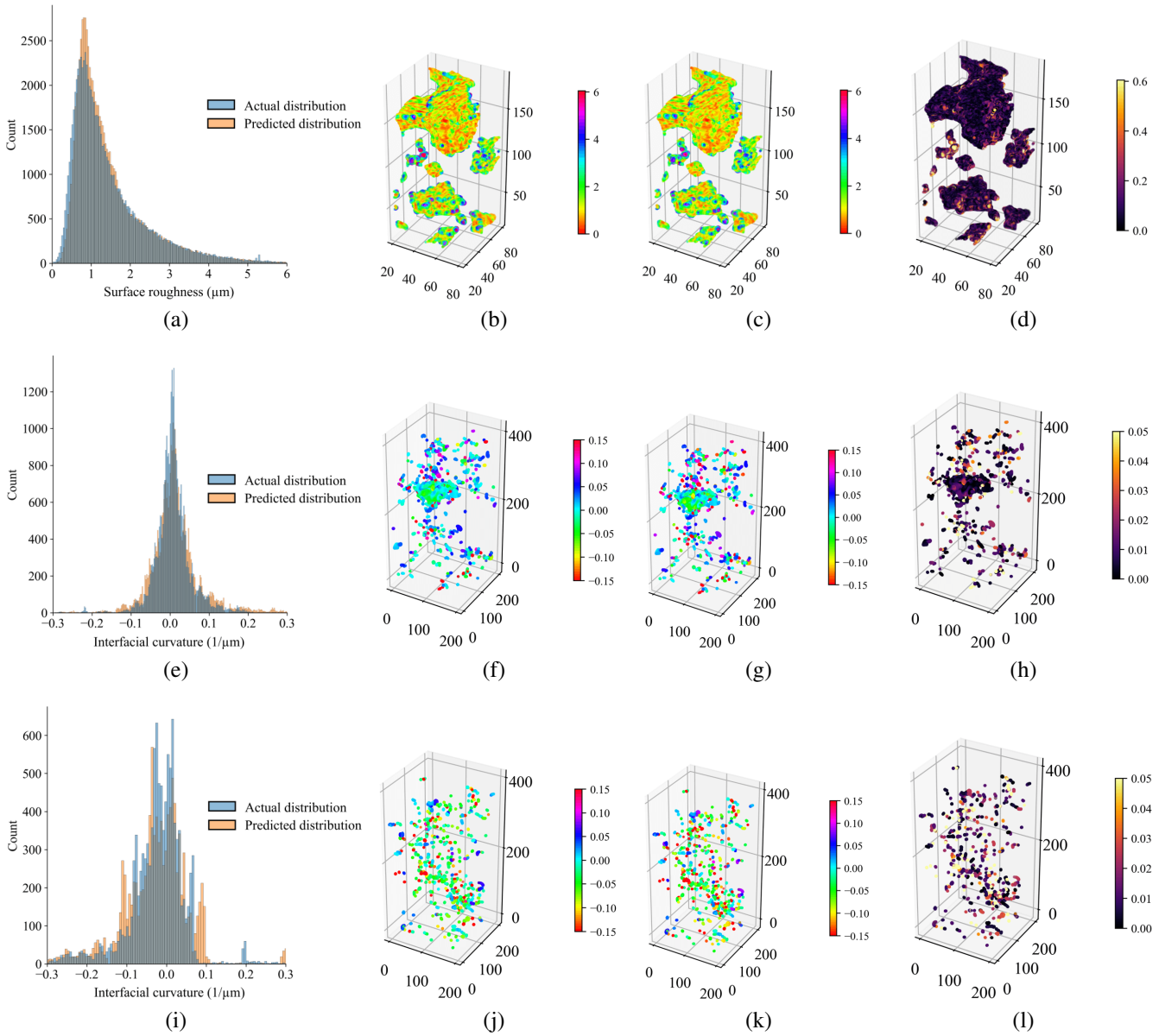


**Fig. 10**. Visualizations of the prediction results of the trained model on unseen testing samples showing the (a)-(d) surface roughness of the LUX sample, (e)-(h) interfacial curvature of the LUX-WW sample and (i)-(l) interfacial curvature of the LUX-MW sample. From left to right, the figure shows the GT and predicted probability distributions, 3D spatial distributions of GT values, model predictions, and absolute differences.

KL sample using the proposed model as well as a comparison with the numerical computation methods. As shown in the table, a reduction of approximately 60% in both inference time and memory requirements can be achieved by the proposed architecture in comparison with traditional methods.

## 4. Conclusions

This paper presents MicroGraphNets, a GNN-based method for the comprehensive characterization of the pore-scale wettability of porous media. In the present approach, various geometric graph representations were constructed to represent the rock surface, fluid-fluid interface, and regions around the 3-phase CL. Two main rocks with varying properties, water-wet BH and oil-wet IL, were considered in the training datasets and their wettability-related properties were computed using published numerical computation methods. In addition, tests were performed on two unseen samples, LUX-WW and LUX-MW, to assess the accuracy of the model on samples that were not included in the training datasets. Graph construction and training for the first two tasks, namely surface roughness and interfacial curvature prediction, are straightforward because (1) it is possible to compute normals and use them as input features, and (2) labels are computed at all nodes. However, estimating the contact angle requires additional data manipulation to include nodes of different types around the 3-phase CLs.

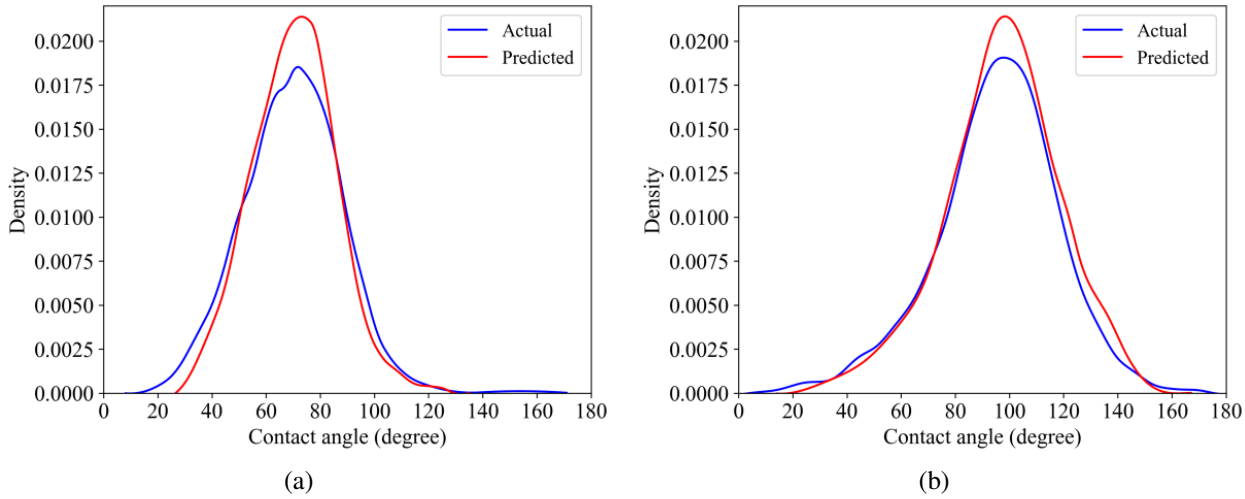


**Fig. 11**. Illustrations of GT and predicted probability distributions of unseen (a) LUX-WW and (b) LUX-MW samples.

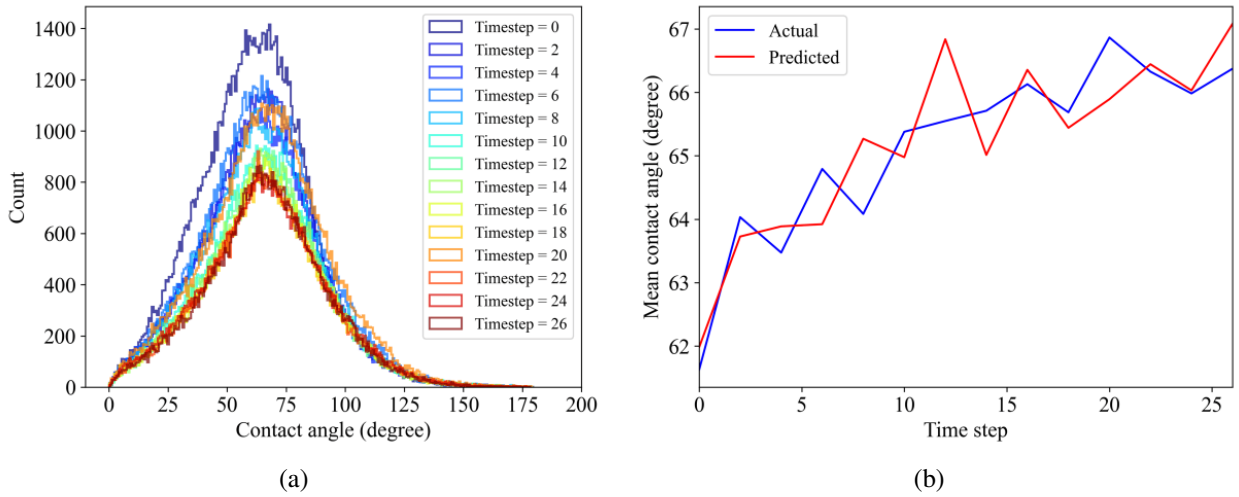


**Fig. 12**. Results of time-resolved analysis of the water flooding experiment performed on the KL sample. The figure illustrates (a) the probability distributions of the contact angles predicted by the proposed model and (b) the GT and predicted evolutions of the mean contact angle at different time steps during the experiment.

The results of this study demonstrate the ability of GNNs to predict surface and interfacial properties accurately and efficiently, with $R^2$ above 0.9 for training datasets and 0.85 for testing datasets. Moreover, the synthetic droplet test validated the accuracy of MicroGraphNets against analytical contact-angle solutions. Finally, a time-resolved analysis was performed to predict the dynamic contact angles at different time steps during the flooding experiment. The findings of this study suggest that GNNs can serve as a suitable substitute for traditional approaches for rapid computation of various surface and interfacial properties. A comprehensive characterization of wettability can aid researchers by enhancing their understanding of multiphase flow behaviors under different wetting conditions as well as helping them build more descriptive numerical multiphase flow simulators. It is recommended that future studies approach more complex and resource-extensive modelling tasks with GNNs, such as multiphase fluid flow simulations, reactive transport, particle tracking, and upscaling from the pore to the core scale.

## Conflict of interest

The authors declare no competing interest.



## References

Alqahtani, N., Alzubaidi, F., Armstrong, R. T., et al. Machine learning for predicting properties of porous media from 2D X-ray images. Journal of Petroleum Science and Engineering, 2020, 184: 106514.

Alqahtani, N. J., Chung, T., Wang, Y. D., et al. Flow-based

characterization of digital rock images using deep learning. SPE Journal, 2021, 26(4): 1800-1811.

Alqahtani, N. J., Niu, Y., Wang, Y. D., et al. Super-resolved segmentation of X-ray images of carbonate rocks using deep learning. Transport in Porous Media, 2022, 143(2): 497-525.

AlRatrout, A., Blunt, M. J., Bijeljic, B. Wettability in complex porous materials, the mixed-wet state, and its relationship to surface roughness. Proceedings of the National Academy of Sciences, 2018, 115(36): 8901-8906.

AlRatrout, A., Raeini, A. Q., Bijeljic, B., et al. Automatic measurement of contact angle in pore-space images. Advances in Water Resources, 2017, 109: 158-169.

Alzahrani, M. K., Shapoval, A., Chen, Z., et al. Pore-GNN: A graph neural network-based framework for predicting flow properties of porous media from micro-CT images. Advances in Geo-Energy Research, 2023, 10(1): 39-55.

Amari, S. I. Backpropagation and stochastic gradient descent method. Neurocomputing, 1993, 5(4-5): 185-196.

Armstrong, R. T., Sun, C., Mostaghimi, P., et al. Multiscale characterization of wettability in porous media. Transport in Porous Media, 2021, 140(1): 215-240.

Ar Rushood, I., Alqahtani, N., Wang, Y. D., et al. Segmentation of X-Ray images of rocks using deep learning. Paper SPE 201282 Presented at the SPE Annual Technical Conference and Exhibition, Virtual, 26-29 October, 2020.

Balaban, S. Deep learning and face recognition: The state of the art. Biometric and Surveillance Technology for Human and Activity Identification XII, 2015, 9457: 68-75.

Boampong, L. O., Rafati, R., Haddad, A. S. Analysis of wettability alteration in low salinity water flooding using a zeta potential-based model. Capillarity, 2023, 7(2): 32-40.

Cai, C., Vlassis, N., Magee, L., et al. Equivariant geometric learning for digital rock physics: Estimating formation factor and effective permeability tensors from Morse graph. International Journal for Multiscale Computational Engineering, 2023, 21(5): 1-24.

Cao, Y., Tang, M., Zhang, Q., et al. Dynamic capillary pressure analysis of tight sandstone based on digital rock model. Capillarity, 2020, 3(2): 28-35.

Charles, R. Q., Su, H., Kaichun, M., et al. PointNet: Deep learning on point sets for 3D classification and segmentation. Paper Presented at the 2017 IEEE Conference on Computer Vision and Pattern Recognition (CVPR), Honolulu, HI, 21-26 July, 2017.

Deng, L., Liu, Y. Deep Learning in Natural Language Processing. Singapore, Springer, 2018.

Chung, J., Ahmad, R., Sun, W., et al. Prediction of effective elastic moduli of rocks using graph neural networks. Computer Methods in Applied Mechanics and Engineering, 2024, 421: 116780.

Diao, Z., Li, S., Liu, W., et al. Numerical study of the effect of tortuosity and mixed wettability on spontaneous imbibition in heterogeneous porous media. Capillarity, 2021, 4(3): 50-62.

Ding, H., Wang, Y., Shapoval, A., et al. Macro-and microscopic studies of "smart water" flooding in carbonate rocks: An image-based wettability examination. Energy & Fuels, 2019, 33(8): 6961-6970.

Fey, M., Lenssen, J. E. Fast graph representation learning with PyTorch geometric. ArXiv Preprint ArXiv: 1903.02428, 2019.

Garfi, G., John, C. M., Berg, S., et al. The sensitivity of estimates of multiphase fluid and solid properties of porous rocks to image processing. Transport in Porous Media, 2020, 131(3): 985-1005.

Geistlinger, H., Golmohammadi, S., Zulfiqar, B., et al. The interplay between pore-scale heterogeneity, surface roughness, and wettability controls trapping in two-phase fluid displacement in porous media. Geophysical Research Letters, 2024, 51(1): e2023GL106197.

Goldberger, J., Hinton, G. E., Roweis, S., et al. Neighbourhood components analysis. Paper Presented at Advances in Neural Information Processing Systems, Vancouver, British Columbia, 13-18 December, 2004.

Haines, W. B. Studies in the physical properties of soil. V. The hysteresis effect in capillary properties, and the modes of moisture distribution associated therewith. The Journal of Agricultural Science, 1930, 20(1): 97-116.

Iglauer, S., Pentland, C. H., Busch, A. $CO_2$ wettability of seal and reservoir rocks and the implications for carbon geosequestration. Water Resource Research, 2015, 51(1): 729-774.

Kashefi, A., Mukerji, T. Point-cloud deep learning of porous media for permeability prediction. Physics of Fluids, 2021, 33: 097109.

Kingma, D. P., Ba, J. Adam: A method for stochastic optimization. ArXiv Preprint ArXiv: 1412.6980, 2017.

Klise, K. A., Moriarty, D., Yoon, H., et al. Automated contact angle estimation for three-dimensional X-ray microtomography data. Advances in Water Resources, 2016, 95: 152-160.

Lourenço, S. D. N., Saulick, Y., Zheng, S., et al. Soil wettability in ground engineering: Fundamentals, methods, and applications. Acta Geotechnica, 2018, 13: 1-14.

Meyer, F., Beucher, S. Morphological segmentation. Journal of Visual Communication and Image Representation, 1990, 1: 21-46.

Otter, D. W., Medina, J. R., Kalita, J. K. A survey of the usages of deep learning for natural language processing. IEEE Transactions on Neural Networks and Learning Systems, 2020, 32(2): 604-624.

Paszke, A., Gross, S., Massa, F., et al. PyTorch: An imperative style, high-performance deep learning library. ArXiv Preprint ArXiv: 1912.01703, 2019.

Rabbani, A., Babaei, M., Shams, R., et al. DeePore: A deep learning workflow for rapid and comprehensive characterization of porous materials. Advances in Water Resources, 2020, 146: 103787.

Rabbani, A., Sun, C., Babaei, M., et al. DeepAngle: Fast calculation of contact angles in tomography images using deep learning. Geoenergy Science and Engineering, 2023, 227: 211807.

Rücker, M., Bartels, W. B., Singh, K., et al. The effect of

mixed wettability on pore-scale flow regimes based on a flooding experiment in ketton limestone. Geophysical Research Letters, 2019, 46(6): 3225-3234.

Santos, J. E., Xu, D., Jo, H., et al. PoreFlow-Net: A 3D convolutional neural network to predict fluid flow through porous media. Advances in Water Resources, 2020, 138: 103539.

Shapoval, A., Alzahrani, M., Xue, W., et al. Oil-water interactions in porous media during fluid displacement: Effect of potential determining ions (PDI) on the formation of in-situ emulsions and oil recovery. Journal of Petroleum Science and Engineering, 2022, 210: 110079.

Shapoval, A., Zhuravljov, A., Lanetc, Z., et al. Pore-scale evaluation of physicochemical interactions by engineered water injections. Transport in Porous Media, 2023, 148(3): 605-625.

Singh, N. S., Hariharan, S., Gupta, M. Facial recognition using deep learning. Paper Presented at International Conference on Data Sciences, Security and Applications, New Delhi, India, 7-8 March, 2019.

Sun, C., McClure, J. E., Mostaghimi, P., et al. Probing effective wetting in subsurface systems. Geophysical Research Letters, 2020, 47(5): e2019GL086151.

Wang, W., Gang, J. Application of convolutional neural network in natural language processing. Paper Presented at 2018 International Conference on Information Systems and Computer Aided Education (ICISCAE), Changchun, Jilin, 6-8 July, 2018.

Wang, Y., Arns, C. H., Rahman, S. S., et al. Porous structure reconstruction using convolutional neural networks. Mathematical Geosciences, 2018, 50(7): 781-799.

Wang, Y. D., Shabaninejad, M., Armstrong, R. T., et al. Deep neural networks for improving physical accuracy of 2D and 3D multi-mineral segmentation of rock micro-CT images. Applied Soft Computing, 2021, 104: 107185.

Yu, Z., Wang, T., Guo, T., et al. Robust point cloud normal estimation via neighborhood reconstruction. Advances in Mechanical Engineering, 2019, 11(4): 1687814019836043.

Yun, W., Liu, Y., Kovscek, A. R. Deep learning for automated characterization of pore-scale wettability. Advances in Water Resources, 2020, 144: 103708.

Zou, S., Sun, C. X-ray microcomputed imaging of wettability characterization for multiphase flow in porous media: A review. Capillarity, 2020, 3(3): 36-44.

Zulfiqar, B., Vogel, H., Ding, Y., et al. The impact of wettability and surface roughness on fluid displacement and capillary trapping in 2-D and 3-D porous media: 2. Combined effect of wettability, surface roughness, and pore space structure on trapping efficiency in sand packs and micromodels. Water Resources Research, 2020, 56(10): e2020WR027965.